New insights into the *P*- and *S*-wave velocity structure of the D″ discontinuity beneath the Cocos plate

Tadashi Kito,[1] Sebastian Rost,[2,3] Christine Thomas[1] and Edward J. Garnero[2]

[1]*Department of Earth and Ocean Sciences, University of Liverpool, Liverpool, UK. E-mail: t.kito@liverpool.ac.uk*
[2]*Department of Geological Sciences, Arizona State University, Tempe, Arizona, USA*
[3]*now at: Institute of Geophysics and Tectonics, School of Earth and Environment, University of Leeds, Leeds, UK*

SUMMARY

Broad-band *P*- and *S*-waves from earthquakes in South America recorded at Californian network stations are analysed to image lateral variations of the D″-discontinuity beneath the Cocos plate. We apply two array processing methods to the data set: a simplified migration method to the *P*-wave data set and a double-array method to both the *P*- and *S*-wave data sets, allowing us to compare results from the two methods. The double-array method images a dipping reflector at a depth range from 2650 to 2700 km in the southern part of the study area. We observe a step-like topography of 100 km to a shallower reflector at about 2600 km depth to the north, as well as evidence for a second (deeper) reflector at a depth range from 2700 to 2750 km in the north. Results from the simplified migration agree well with those from the double-array method, similarly locating a large step in reflector depth in a similar location (about 2650 km depth in the south and about 2550 km in the north) as well as the additional deeper reflector at the depth of about 2750 km in the north. Waveform modelling of the reflected waves from both methods suggests a positive velocity contrast for *S* waves, but a negative velocity contrast for *P* waves for the upper reflector in agreement with predictions from mineral physical calculations for a post-perovskite phase transition. The data also show some evidence for the existence of another deeper reflector that could indicate a double intersection of the geotherm with the post-perovskite stability field, that is, the back-transformation of post-perovskite to perovskite close to the core–mantle boundary.

Key words: D″ discontinuity, seismic array.

1 INTRODUCTION

A rapid increase in the availability of seismic data over the last decade has facilitated a wealth of exciting discoveries of structural features in the lowermost mantle and core–mantle boundary (CMB) region (e.g. see Wysession 1996; Lay *et al.* 1998; Garnero 2000; Kendall 2000; Masters *et al.* 2000; Wen *et al.* 2001; Lay & Garnero 2004). The resolution of seismic studies now allows routine comparisons between seismic results and those from other disciplines to decipher the thermal, chemical and dynamical state of the Earth's deep interior (e.g. Williams *et al.* 1998; Sidorin *et al.* 1999a,b; Buffett *et al.* 2000; Rost & Revenaugh 2001; Helffrich 2002; Lay *et al.* 2004a, 2005; Thomas *et al.* 2004; Hernlund *et al.* 2005). Thus, ample evidence now exists that shows that the CMB is far more complex than a simple, 1-D discontinuity between the silicate rock mantle and liquid iron-alloy outer core.

Recent applications of seismic array methods to high-quality data from seismic arrays and networks targeting the deep mantle find small-scale structures at the CMB on scale-lengths from a few tens to a few hundred kilometres with strong variations both laterally and vertically (e.g. see Weber 1994; Lay & Young 1996; Earle & Shearer 1997; Revenaugh & Meyer 1997; Scherbaum *et al.* 1997; Vidale & Hedlin 1998; Castle *et al.* 2000; Persh *et al.* 2001; Kito & Krüger 2001; Rost & Revenaugh 2001, 2003; Braña & Helffrich 2004; Kito *et al.* 2004; Thomas *et al.* 2004b; Rost *et al.* 2005). The densification and availability of permanent and temporary array deployments (Rost & Garnero 2004) allows increased application of stacking algorithms that enhance the signal-to-noise ratio (SNR) of coherent arrivals over incoherent noise (e.g. Rost & Thomas 2002) allowing analysis of subtle arrivals and waveform variations to study the fine-scale structure of the CMB.

Due to the source–receiver geometry between deep South American earthquakes and dense broad-band networks in California, the region beneath western Central America (i.e. the Cocos plate) constitutes a perfect experimental setting for the study of deep Earth structure, which has been probed by a variety of different approaches (e.g. Lay & Helmberger 1983; Kendall & Shearer 1994; Reasoner & Revenaugh 1999; Garnero & Lay 2003; Lay *et al.* 2004b; Rokosky *et al.* 2004; Thomas *et al.* 2004b; Hutko *et al.* 2006), often yielding contrasting results (e.g. Lay & Helmberger 1983; Kendall & Shearer

© 2007 The Authors
Journal compilation © 2007 RAS

631

Table 1. Past D″ studies in Cocos Plate, Central America, Caribbean study region.

Study	Data type	D″ thickness (km)	Velocity Jump (per cent)	Comments
Mitchel & Helmberger (1973)	S, ScS	40–70	4–7	
Lay & Helmberger (1983)	S, SdS, SDS, ScS	250	2.75	Model SLHA
Zhang & Lay (1984)	S, SdS, ScS	251	2.71	
Weber & König (1992)	P, PdP, PcP	340	2–3	
Kendall & Shearer (1994)	S, SdS, ScS	140–370	2.75	D″ Thickness variable
Kendall & Nangini (1996)	S, SdS, ScS	250, 290	2.45, 2.75	D″ Thickness variable
Kendall & Nangini (1996)	S, SdS, ScS	250	2.75	Anisotropy
Ding & Helmberger (1997)	S, SdS, SDS, ScS,	200	3.0 (S),	
	P, PdP, PcP	———	<1 (P)	
Reasoner & Revenaugh (1999)	P, PdP, PcP	190	0.5–0.6	
Garnero & Lay (2003)	S, SdS, ScS	n/a	n/a	D″ discontinuity and anisotropy detected,
Lay *et al.* (2004b)	S, SdS, ScS	264	0.9–2.6	Lateral variation of D″ velocity
Rokosky *et al.* (2004)	ScSV, ScSH	250	n/a	Vertical Transverse isotropy up to 0.63 per cent
Thomas *et al.* (2004b)	S, Sscat*, ScS	150–300	n/a	Lateral variation of D″ thickness
Rokosky *et al.* (2006)	ScSV, ScSH	250	n/a	Variable azimuthal anisotropy
Hutko *et al.* (2006)	S, Sscat*, ScS	150–300	n/a	Lateral variation of D″ thickness
Thorne *et al.* (2006)	SH synthetics	264	0.9–2.6	

Sscat * = Scattered waves from heterogeneities in D″.

1994; Kendall & Nangini 1996; Ding & Helmberger 1997; Garnero & Lay 2003). A summary of the results for this region is given in Table 1.

Recent studies for this region using *ScS* core reflected phases show evidence for strong topography of about 150 km on the *S* wave D″ discontinuity (Thomas *et al.* 2004, 2004b) with the strongest topography gradient around 5°N latitude. Another study using *S* waves (Hutko *et al.* 2006) targeting the same region of the lower mantle proposes that the topography is a sharp step in the post-perovskite phase transition (Murakami *et al.* 2004; Oganov & Ono 2004) due to the temperature perturbation from a subducted slab folding and bending atop of the CMB and displacing a thin and hot boundary layer (Hutko *et al.* 2006). The deep mantle in the study region is characterized by high seismic velocities in tomographic studies (e.g. Boschi & Dziewonski 1999; Ritsema & Van Heijst 2000; Gu *et al.* 2001; Karasón & van der Hilst 2001; Becker & Boschi 2002; Grand 2002), perhaps supporting the existence of subducted oceanic lithosphere at D″ depths (e.g. Grand *et al.* 1997; Lithgow-Bertelloni & Richards 1998) as proposed by Hutko *et al.* (2006).

These seismic models are extremely important for the interpretation of the phase transition from perovskite to post-perovskite, which is extensively discussed as possible source for the D″ discontinuity. Mineral physical modelling (Wookey *et al.* 2005) of the phase transition predicts a strong discontinuity of approximately 4 per cent for *S*-waves, but only a very weak discontinuity of approximately 0.5 per cent for *P* waves. A detailed analysis of both *S*- and *P*-wave structure of the discontinuity in this region can shed further light on the importance of the post-perovskite phase transition for the structure of the D″ discontinuity. Here, we present a joint *S*- and *P*-wave analysis of this region to resolve the discontinuity structure for both wave types simultaneously.

Studies of this region have predominantly exploited *S*-wave information, which indicate an abrupt velocity increase about 200–300 km above the CMB. There are strong trade-offs between the topography and the velocity structure of D″ (Lay *et al.* 2004b; Thomas *et al.* 2004b). Using an identical data set they find a best fit to the data either by a constant discontinuity depth of 264 km above the CMB with laterally varying D″ velocity increases from 0.9 to 2.6 per cent (Lay *et al.* 2004b) or by constant velocities in D″ with discontinu-

ity topography from 300 to 150 km (Thomas *et al.* 2004b). Using a Kirchhoff migration technique targeting the same study area, a sharp step of the *S*-wave discontinuity from 60 to 190 km above the CMB in the southeast to 250–290 km above the CMB in the northwest of the study region has been resolved (Hutko *et al.* 2006). They also find evidence for out of plane scattering, which could explain the detection of the lower reflector in Thomas *et al.* (2004b). Tests with synthetic seismograms show that the assumed one-dimensionality of these structures is not adequate and that 3-D waveform effects have to be taken into account to explain the recorded data (Thorne *et al.* 2006).

Few *P*-wave studies of this region exist (Table 1). Reasoner & Revenaugh (1999) detect a weak (1 per cent velocity contrast) *P*-wave discontinuity in this region at depths ∼190 above the CMB, while Ding & Helmberger (1997) find little evidence for a *P*-wave discontinuity (suggesting the *P* discontinuity must be weaker than approximately 1 per cent, the detection threshold in that study). In summary, these previous studies show clear evidence for an *S*-wave discontinuity, while the evidence for a *P*-wave discontinuity is weak. The exact depth location and strength of this discontinuity varies due to the trade-off between seismic velocities and layer thickness, the possibly strong 3-D structure, different reference structures and modelling approaches. There remains a strong uncertainty in the structure of the discontinuity in this location.

The region beneath the Cocos plate also shows evidence for seismic anisotropy. Kendall & Nangini (1996) and Garnero & Lay (2003) indicate the presence of D″ anisotropy over the greater Central America and Caribbean region. Rokosky *et al.* (2004) detect vertical transverse isotropy (VTI) with an average value of 0.63 per cent. Evidence for azimuthal anisotropy is also present (Garnero *et al.* 2004; Maupin *et al.* 2005), which may have geographical variations that correlate to mapped D″ topography (Rokosky *et al.* 2006).

Array methods are well suited to study the structure of the D″ discontinuity (e.g. Reasoner & Revenaugh 1999; Thomas *et al.* 2004b; Hutko *et al.* 2006). Here, we apply two different array methods (Kito *et al.* 2004; Thomas *et al.* 2004, 2004b) to Californian *P*- and *S*-wave recordings from South American earthquakes, in an effort to better understand possible biases in the different array approaches
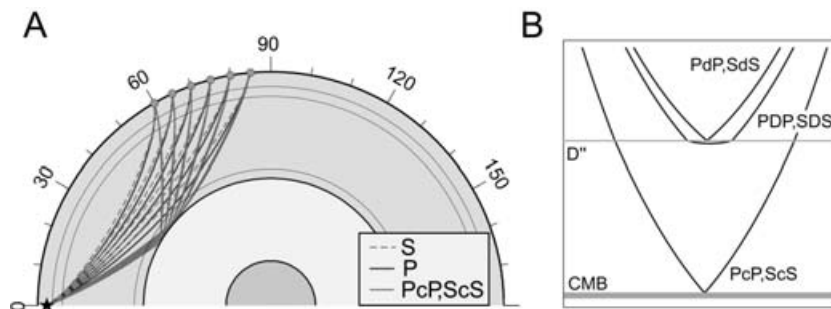
Figure 1. (a) Ray paths for *PcP* and the reflection at the top of D″ (∼300 km above the CMB) *PdP* phase, the shifted overcritical reflection as well as the diving wave *PDP*. (b) Ray paths for *ScS* and the post-critical refracted phase *SDS* (*Scd*) and phase-shifted post-critical reflected phases *SdS* (*Sbc*).

and search for evidence for both *P-* and *S-wave* velocity discontinuities beneath the Cocos plate. We use core reflected *ScS* and *PcP* phases and their precursors, *SdS* and *PdP* due to the reflection off the D″ discontinuity (Fig. 1) to probe D″ structure. At distances greater than ∼75°, refraction in the high velocity D″ layer becomes important. This energy has been noted as *SDS* and *PDP*, or *Sbc* and *Pbc,* for *S-* and *P* waves, respectively. In this paper, we will adopt the *PdP* and *PDP* convention (similarly for *S*).

The combined approach of using *P-* and *S-wave* information and using different analysis methods will allow us to compare the sensitivity of the array approaches. Comparison of the possible resolution of the D″ discontinuity will further help to get a better understanding of the origin of the D″ discontinuity.

2 DATA AND METHODS

2.1 California network *P-* and *S-wave* data

Broad-band data have been collected from two seismic networks in California: TRINET (a network jointly run by the California Institute of Technology, the U.S. Geological Survey, and the California Geological Survey) and Berkeley Digital Seismic Network (BDSN). We use nine and 13 large intermediate depth South American subduction zone events for the *P-* and *S-wave* study, respectively (Fig. 2). The earthquake-station configuration was selected to allow a dense sampling of the lower mantle for both *P* and *S* waves, and samples D″ beneath the Cocos Plate. The source parameters of events used in this study are listed in Table 2; epicentral distances are between 61° and 86°, however, most of the station-event distances are between 70° and 75°.

To obtain a clean recording time window for the core reflected phases *ScS* and *PcP*, we select earthquakes with sources deeper than 100 km. For shallower events the depth phases (*pP*, *sP*, *sS* and *pS*) contaminate the *PcP* and *ScS* observational time window, making the detection of possible precursors generated from the reflection off the D″ discontinuity (or heterogeneity) difficult. Only recordings with clean and impulsive *P* and *S* waves containing high SNRs were retained in our study; low quality recordings (high-noise level, spikes, recording errors and local seismicity) were discarded. The final data set consists of 767 *P-* and 261 *S-wave* traces, which we use in our array processing experiments. Owing to the different event distribution for the *P-* and *S-wave* study, the *S-wave* coverage of the CMB with reflection points is larger than for *P* (Fig. 2), with *P-wave* coverage extending over the central part of the area sampled by *S* waves. The focal mechanisms of the events are plotted in Fig. 2 and it is noted that no nodal lines split *P* and *PcP* takeoff angles. We could exclude the possible reversed polarity of
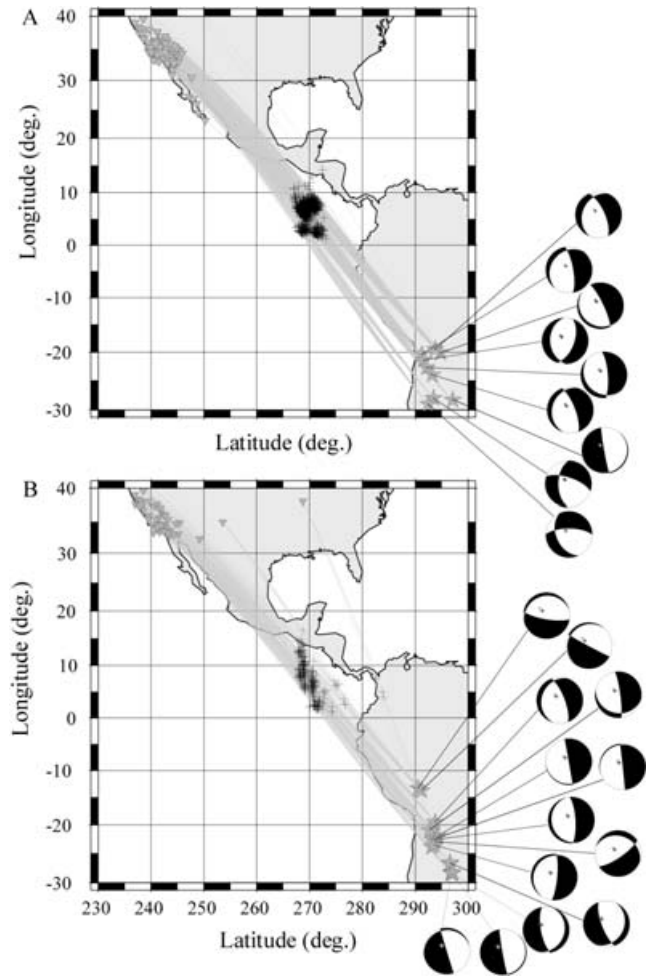

Figure 2. (a) Source–receiver combination for the *P-wave* study. Earthquakes are shown as stars and the stations of the Southern California network are shown as triangles. The *PdP* CMB reflection points are marked with crosses. *P* and *PcP* take-off angles are marked with light and dark grey crosses on the focal mechanisms, respectively. The source parameters are taken from Harvard CMT solutions for the focal mechanisms. The takeoff angle of PdP would lie between *P* and *PcP*. (b) Source–receiver combination for *S-wave* study. Symbols are selected as in (a).

PdP due to the focal mechanisms. The parameters have been taken from NEIC Preliminary Determinations of Epicentres (PDE) catalogue and possible errors (less than ±10 km for most events) of the source location are within our depth resolution in the lower mantle.

Table 2. Event used in this study. The parameters have been taken from NEIC PDE (Preliminary Determinations of Epicentres) catalogue.

Event number	Date (yyyy-mmm-dd)	Latitude (°)	Longitude ((°))	Depth (km)
P waves				
1	2000-April-23	−28.38	−62.94	609.0
2	2000-June-14	−24.03	−66.75	196.0
3	2001-March-16	−20.41	−68.74	115.0
4	2001-April-21	−29.10	−67.52	127.0
5	2001-May-15	−28.06	−66.55	176.0
6	2001-June-19	−22.74	−67.88	146.0
7	2001-June-29	−19.52	−66.25	273.0
8	2003-July-27	−20.13	−65.18	345.0
9	2003-September-17	−21.47	−68.32	127.0
S waves				
1	1993-May-24	−22.67	−66.54	221.0
2	1993-October-19	−22.38	−65.97	272.0
3	1994-January-10	−13.34	−69.45	596.0
4	1994-April-29	−28.30	−63.25	561.0
5	1994-May-10	−28.50	−63.10	600.0
6	1994-August-19	−26.64	−63.42	564.0
7	1997-January-23	−22.00	−65.72	276.0
8	1997-July-20	−22.98	−66.30	256.0
9	1997-November-28	−13.74	−68.79	586.0
10	1999-September-15	−20.93	−67.28	218.0
11	2000-April-23	−28.38	−62.94	609.0
12	2000-May-12	−23.55	−66.45	225.0
13	2001-June-29	−19.52	−66.25	273.0

2.2 Data processing

This section describes all processing that was applied to the data before using the two array stacking methods, which are described in more detail in the following sections. All traces are aligned on the first *P* (or *S*) arrival to suppress traveltime variations due to small-scale heterogeneity beneath the individual stations and height differences between stations. For *S* waves, horizontal component records were deconvolved with the instrument responses and rotated to the great circle path to obtain transverse components of motion. For *P* waves, the vertical component trace is used.

Due to the short traveltime difference between *P* (*S*) and *PcP* (*ScS*) the coda of the first arrivals (*P* and *S*) might interfere with the later arriving core (*PcP* and *ScS*) and D″ (*PdP* and *SdS*) reflections, a common source wavelet for *P* for each event is calculated by the alignment of all stations. The *P* beam wavelet is cut from the onset time to the end of *P* coda and then each trace is divided by the *P* beam wavelet in the frequency domain event by event using a water level of 1.0^{-6} in order to obtain deconvolved seismograms. The processing is similarly done for *S* waves. *P* and *PdP* (*S* and *SdS*) have similar traveltimes and moveout for distances larger than 80 d. The differential traveltime of *P* and *PcP* is around 6 s and around 17 s for *S* and *ScS* for distances of 80° and *PdP* (*SdS*) should arrive between *P* (*S*) and *PcP* (*ScS*) in time depending on reflector depth. This makes it difficult to separate the phases in this distance range; thus data in this distance range were not considered in our analysis. Furthermore, event-station configurations with CMB reflection points located east of 274°, that is, outside our most dense D″ sampling (see Fig. 2), were omitted in order to restrict ourselves to the most densely sampled D″ region. Individual data were normalized to the maximum amplitude of the reference wave (either direct *P* or *S*) in each trace prior to deconvolution to equalize the energy contribution towards stacked waveforms. Example raw seismograms are shown in Fig. 3. Traces are sorted by epicentral distance and aligned on direct arrival (*P* and *S*). Core-reflected *ScS* arrivals are clearly visible, while *PcP* cannot be identified in the raw data. The *PcP* CMB reflection coefficient for this distance range is rather small (typically 13 per cent relative to direct *P*, for *P* and *PcP* energy radiating with equal amplitude from the source for the model IASP91, Krüger *et al.* 1995). *SdS* often shows large amplitudes above the noise level even in raw data. Nonetheless, the data example does not show any coherent arrival between *ScS* and *S* that could be identified as *SdS*. Array processing is often necessary to raise these arrivals above the noise level.

Our array processing assumes purely reflected energy as the source of all additional arrivals in the wavefield. Since the *PcP* and *ScS* precursor wavefields for postcritical distances contain both reflected (*PdP* or *SdS*) and refracted (or diving wave, *PDP* or *SDS*, Fig. 1) energy, a careful inspection is necessary to insure how the arrival times of *PDP* or *SDS* are different from those of *PdP* or *SdS*. Also, it is important to note that *PdP* and *SdS* experience a phase shift for larger distances due to overcritical incidence independent of *PDP* and *SDS*. Tests with synthetic seismograms show that for this study (with most epicentral distances less than 75°) traveltimes of *PdP* and *PDP* (*SDS* and *SdS*) are nearly identical (Wysession 1998), so that we refer to the combined energy of these two arrivals as *PdP* (and *SdS*).
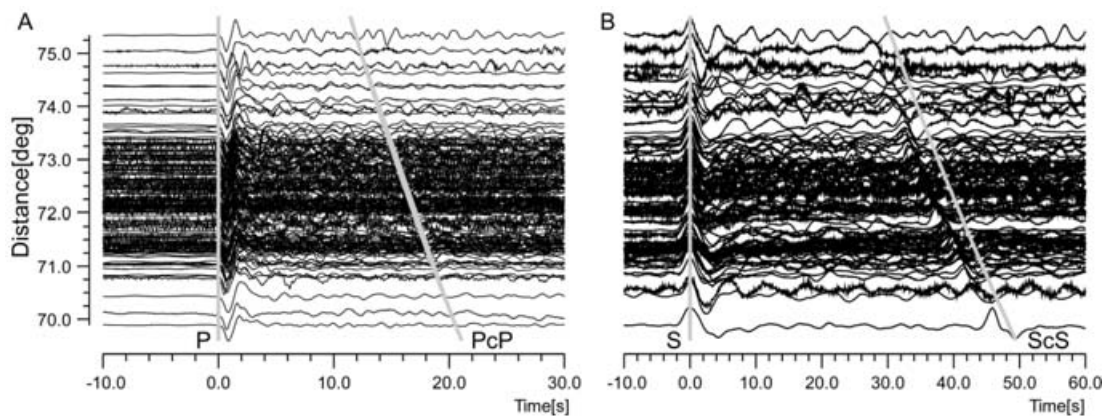

Figure 3. (a) *P*-wave seismograms from event on 2001 June 29 (18:35 UT). Traces are aligned on the *P* arrival and sorted by epicentral distance. Amplitudes are normalized to the direct *P*-wave amplitudes. The data are unfiltered. The grey lines indicate the theoretical traveltime of *P* and *PcP* for the 1-D earth model ak135 (Kennett *et al.* 1995) after alignment on the *P* arrival. (b) As A but for *S*-wave seismograms for the same event. Grey lines mark the aligned *S*-wave arrival and the *ScS* arrival relative to *S* for ak135.
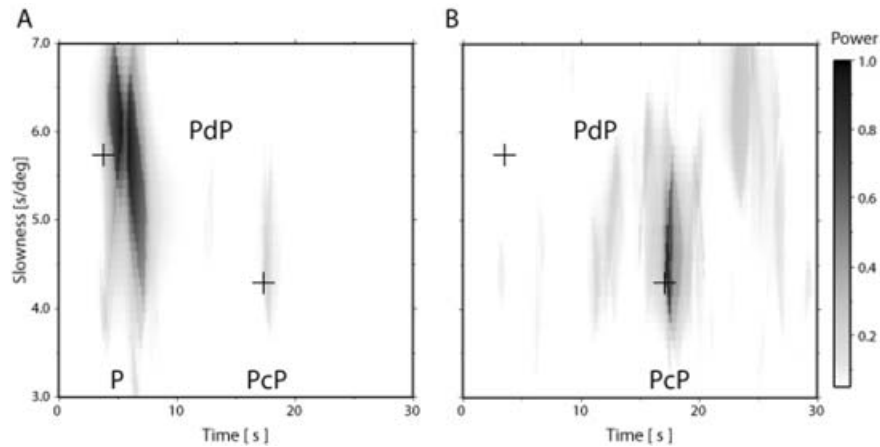
Figure 4. Vespagrams of traces sampling the latitudinal area from 1°N to 5°N for the event on 2000 June 14 (event 2 in Table 2). (a) *P*-wave vespagram with *P* wavelet included. Large amplitudes of *P* make the detection of *P*-wave coda difficult, although energy can be detected between *P* and *PcP*. Crosses indicate slowness and traveltime of *P* and *PcP*. (b) *P*-wave vespagram with *P*-wavelet removed: The smaller phases (such as *PdP* and *PcP*) can be detected better due to the removal of the large *P* wavelet.

Since *PcP* cannot be identified in individual traces (Fig. 3a) we use *P* as reference phase for this study. Although *ScS* can be clearly identified (Fig. 3b), for consistency we also use *S* as reference phase for the *S*-wave investigation. The lower and mid-mantle in our study region is characterized by high-velocities in tomographic *P*- and *S*-wave studies (e.g. Boschi & Dziewonski 1999; Ritsema & Van Heijst 2000; Karasón & van der Hilst 2001; Gu *et al.* 2001; Grand 2002), thus we can expect traveltime perturbations of our reference phase (*P* or *S*) resulting in defocused stacks for *PcP* and *ScS* energy. Therefore, we apply traveltime corrections to our data based on predictions from tomographic models of mantle heterogeneity before stacking. For the *P*-wave study we use the model by Karasón & van der Hilst (2001), and for the *S*-wave study the model by Grand (2002). The traveltime corrections for these models range from −0.49 to 0.13 s for the *P* wave and from −2.53 to 1.81 s for the *S*-wave data set. Although these values are not significant enough to correct traveltime bias caused by 3-D heterogeneities completely, the traveltime correction is still worth applying to reduce the traveltime residuals.

We calculate vespagrams (Davies *et al.* 1971) from the raw data to check for *PcP* and *PdP* arrivals in the stacked data. Fig. 4 shows vespagrams of the *P* wave and its coda. The *PdP* amplitudes are small compared to the direct *P* wave (Fig. 4a), so that the arrival cannot be clearly identified with this basic array processing. However, the *PdP* arrival becomes much clearer in the vespagram when the *P* wavelet is removed from the seismograms before stacking by subtracting the *P* beam (Fig. 4b). Vespagrams are normalized by the maximum amplitudes within the plot area, resulting in the different scale for the images with and without *P*-wavelet subtraction. This detection of the *PdP* using the simple vespagram method motivates us to apply more advanced array techniques to the data. In what follows we describe more advanced array processing approaches to resolve smaller scale D″ structure from these *PdP* arrivals. We will compare two array methods (Kito *et al.* 2004; Thomas *et al.* 2004, 2004b) to understand D″ structures more comprehensively and to figure out possible bias caused by different array methods.

2.3 Double-array stacking method

Double-array stacking method (DAM) (Kito *et al.* 2004) is applied to the *P*- and *S*-wave data set discussed above. The DAM uses source and receiver arrays simultaneously to increase the SNR of coherent arrivals and reduce amplitudes of phases generated by heterogeneities close to the individual sources (which arrive coherently at the receiver array). It is especially useful to enhance phases originating from the lowermost mantle that are coherent for both, source and receiver, arrays (Krüger *et al.* 1996; Revenaugh & Meyer 1997). The DAM further increases the SNR of coherent arrivals, since the SNR in the DAM is proportional to the square root of the number of sources times receivers compared to the square root of receivers for pure receiver array stacking. Nonetheless, source mislocation and traveltime variations due to receiver side structure can cause incoherency of the wavefield in the stacking process. Therefore, traveltime corrections are more essential for successful application of the DAM than in the case of single array methods. The traveltime bias caused by these uncertainties often amount to the order of 1 s for teleseismic sources. Therefore, the traveltime residual must be corrected properly before applying DAM. For more details on the method see Kito *et al.* (2004) and Krüger *et al.* (1996). To use several sources simultaneously the sources must be normalized which is done by source deconvolution as described above, which results in a simple impulse-like source–time function for each event. The DAM projects energy back to a suite of assumed reflector depths located at the ray path midpoints. Stacks were performed at depth intervals of 5 km over the depth range from 2300 to 3000 km. The source-deconvolved, direct *P* or *S* masked traces were shifted with respect to the theoretical traveltimes of the reflected waves off each hypothetical interface in this depth range. The theoretical traveltimes were calculated based on the 1-D velocity model ak135 (Kennett *et al.* 1995), while accounting for the curvature of the Earth's surface. To get higher resolution in the stacks we calculate the Phase Weighted Semblance Beam Power (PWSEMBP) (Kito *et al.* 2004) using the Phase-Weighted-Stacking technique (Schimmel & Paulssen 1997) as an amplitude independent measure of the signal coherency across the array. The PWSEMBP is a multiplication of the results of the power of conventional beamforming, the semblance process (Taner & Koehler 1969) and Phase-Weighted-Stacking (PWS). Beam power and semblance are dependent on absolute amplitudes and amplitude differences among traces, respectively. PWSEMBP reduces incoherent, large-amplitude signals and enlarges coherent, small amplitude arrivals. Therefore, it is well suited to detect potential reflections, such as *PdP* and *SdS,* from deep

mantle reflectors. We select time windows of 3 and 6 s for *P* and *S* waves, respectively, to calculate the PWSEMBP. The time windows are tapered using a Gaussian function with the same width of the time windows (3 and 6 s for *P* and *S* waves) before stacking.

To study lateral variations of D″ structure, the study area was subdivided in seven bins for the *P*-wave study. Since more events with a slightly different source distribution are used, the *S*-waves sample a larger region of the CMB and we use 13 bins for the *S*-wave study. The bin size is determined in terms of the stability of the stacked waveforms. Since the *S* waves have longer period energy and are, therefore, more coherent, the stacked waveforms are more stable those of the *P* waves in our data set. Taking this into consideration latitudinal bin sizes are 4° for *P* waves and 2° for *S* waves, respectively. Due to a different distribution of reflection points for *P* and *S* waves, bins cover the latitudinal area from 0°N to 10°N for *P* waves and up to 14°N for *S* waves. Due to a shift of 1° between bins, the individual bins overlap somewhat. All traces with reflection points in an individual bin are stacked simultaneously and the PWSEMBP is calculated for all bins for reflector depths from 2300 to 3000 km. The results for the DAM for *S* and *P* waves are shown in Fig. 5. The *S*-wave data were low pass butterworth filtered with a corner frequency of 3 s and order 2, the *P* waves were filtered with a bandpass butterworth filter 2–50 s (order 2). The lower cut-off frequency was selected to avoid long-period noise. In the frequency band below 3 s (Fig. 5a) a distinct positive velocity discontinuity for *S* waves can be seen at a depth of ∼2600 km. The results show an abrupt step at 4°N where the discontinuity drops from 2600 to 2730 km. In the DAM method the middle of a high-amplitude region is used to measure the depth of the reflector.

The PWSEMBP is normalized to the maximum amplitude in the stacks between 2400 and 2800 km depth. The normalization helps preventing incorrect estimates for *SdS* amplitudes due to fluctuations in *ScS* energy. Since the normalization works on individual bins the absolute *ScS* energy varies somewhat between the bins. The energy

that maps into depths shallower than 2500 km can be attributed to contamination from the *S* wavelet that was not removed by the masking process with the common source wavelet. This energy is mainly due to *S*-wave coda generated by crustal reverberations and velocity heterogeneities at the source and/or receiver array. The stacks show an apparent topography of the CMB of about 50 km between individual bins. This is mainly due to an incomplete correction of the traveltimes of *PcP* and *ScS* by the tomography correction, suggesting that the velocity increase in the high velocity D″ layer is larger than given by the tomographic models. The study area is located in the transition zone between a region with insignificant *S*-wave velocity reductions (*dVs* ∼ 0.5 per cent) and a high-velocity (+1.5 per cent) region (Grand 2002). The velocity perturbation increases towards the north in good agreement with the mapped CMB topography, which is apparently shallower in this region. A comparison with the *S*-wave results of Thomas *et al.* (2004b) (black circles in Fig. 5a) shows a good agreement between the two independent array approaches. There is an indication of a second, lower reflector beneath the northern part of the study area coinciding with the negative reflector found by Thomas *et al.* (2004b). In Fig. 5(a) there might also be some evidence for scattering beneath the upper reflector which could be due to the averaging process of different reflector depths within a latitudinal bin (see results of the upper reflector from the migration method below).

Although past *P*-wave studies of this region (e.g. Ding & Helmberger 1997; Reasoner & Revenaugh 1999) suggested only a very weak (or undetectable) *P*-wave discontinuity, the PWSEMBP is able to detect a clear *PdP* signal from a *P*-wave discontinuity at a depth of ∼2550 km (Fig. 5b). Similar to the result for *S*-waves the *P*-wave discontinuity seems to indicate a step-like increase in discontinuity depth at a similar location at approximately 4°N latitude. In addition, the second, lower discontinuity is visible in *P*-wave data. Again, the energy that stacks coherently for depths less than 2500 km is probably due to *P* coda energy which has not been subtracted by the
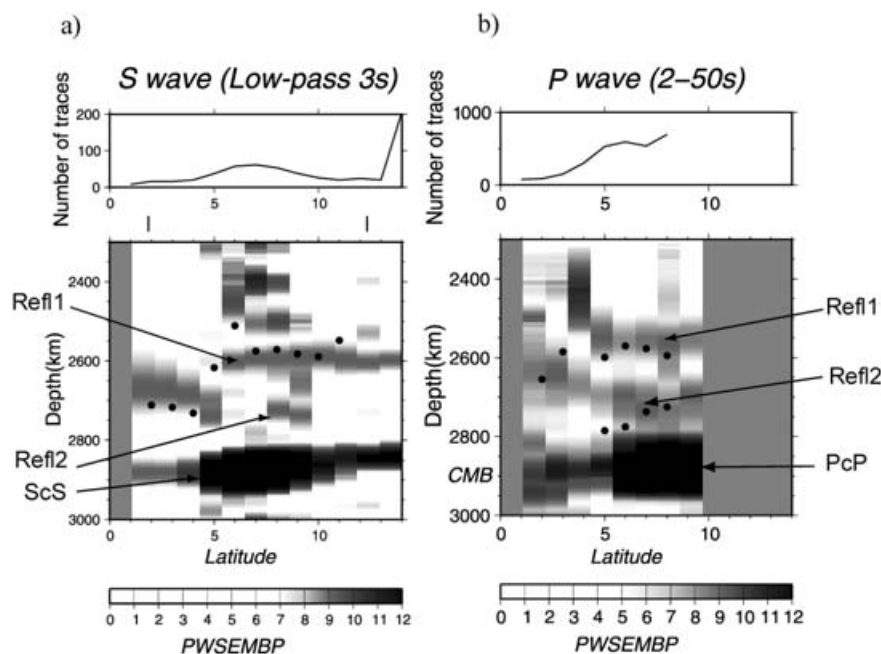
Figure 5. (a) PWSEMBP results for *S* waves of data for a 3 s low-pass filter of order 2. Results from Thomas *et al.* (2004b) are indicated by black circles. The large reflection around 2900 km is the CMB reflection. Coherent energy above 2500 km is most likely due to the remains of the direct *S* wave. (b) Same as (a) but for *P* waves with bandpass filter 2–50 s, order 2. The *PcP* reflection is found at around 2900 km. The large energy above 2500 km is likely to be remains of the *P* wave. Black circles are the results from the migration method, as shown below.

P common wavelet subtraction. A strong *P*-wave discontinuity at these mid-mantle depths is unlikely. The black circles in Fig. 5(b) show the results from the migration method described later, averaged into latitudinal bins (see below) and show good agreement for the upper reflector. Nonetheless, there are some discrepancies in the location of the lower reflector as will be discussed later.

2.4 3-D grid migration method

We migrate the events with a simplified isochrone migration method, so migrating for points with constant traveltime, similar to the one described by (Thomas *et al.* 1999, 2004, 2004b) where it was applied to an *S*-wave data set sampling the same study region (Thomas *et al.* 2004b). Here we will only describe the basic processing techniques. In contrast to the DAM the migration was only applied to the *P*-wave data set since the *S*-wave results are described in Thomas *et al.* (2004b). The *P*-wave data were filtered as described above with a bandpass with corner frequencies of 2 and 50 s. We migrate to a grid in the lower mantle with a grid spacing of 1° in both longitude and latitude. The grid spans the area from −2° to 10° latitude and 260° to 280° longitude and the vertical grid spacing is 10 km from 2985 to 2205 km depth. The grid extends into the outer core to detect defocusing of *PcP* due to lower mantle velocity heterogeneities that could lead to a focusing depth of *PcP* below the CMB. For gridpoints below the CMB the *P*-wave velocity of the last mantle layer in ak135 (Kennett *et al.* 1995) is used. Each gridpoint represents the location of a potential reflector (or scatterer) in the lower mantle. With these grid dimensions nearly 30 000 potential reflector locations are studied for each source–receiver combination. This method migrates event by event in contrast to the DAM method, which utilizes all sources and receivers at the same time. Individual traces are shifted with respect to traveltimes calculated from earthquake to gridpoint and gridpoint to individual station. We use the 1-D earth model ak135 (Kennett *et al.* 1995) to calculate these traveltimes and apply a tomographic correction (Karasón & van der Hilst 2001). After time shifting traces accordingly, the traces are stacked and the resulting amplitude is measured in a time window of 3 s around the theoretical arrival of a potential scatterer from this gridpoint, that is, a potential *PdP*. Although, we use tomographic corrections to account for possible 3-D structure, we are aware that the tomographic models only represent a smoothed long-period version of the Earth structure and our corrections might not be sufficient especially in our study region where strong velocity heterogeneities are detected.

It is important to note that the DAM averages the results in bins along a latitudinal line and provides a 2-D picture of the structure whereas the migration method displays a 3-D picture of the imaged area since the results are displayed at the reflection points for each source–receiver combination. In order to compare the two methods, the migration results will have to be averaged latitudinally. To obtain stable results in the migration, a minimum population of the bins is necessary. It has been found that stable results can be obtained with at least seven records in each bin (Thomas *et al.* 2004b). We use the same criterion and vary the bin size somewhat to ensure the minimum number of traces for each bin. In total 26 bins are well populated and can be studied.

Fig. 6 shows the results of the migration in two cross-sections, one perpendicular to the great circle path and one along the great-circle path. We also show a stacked amplitude–depth profile. This amplitude–depth profile measures the amplitude at the theoretical reflection point and the largest amplitude within the 1 s Fresnel

zone and displays it against the depth of the layer. In both the cross-sections and the amplitude–depth profile, energy from *PdP* is visible at approximately 2635 km depth.

Migrating a delta function waveform will focus the energy into a singular point indicating the resolved reflector depth. The energy will focus into one high amplitude precursor at the reflector depth and will smear out along an isochrone for shallower depths. The limited bandwidth of the data used in this study will lead to a slightly different scenario with broader energy maxima in the migrated stacks manifest as high stack amplitudes smeared over a depth interval. In this case the focusing point of the phase will be at the deepest depth of the high amplitude region, that is, the point of the waveform with the longest traveltime in agreement with the synthetic tests (Fig. 7). The waveforms used in this study generally show a two-sided wavelet, which complicates the reflector detection even further due to the waveform interference of the wavelets in the migration. The reflector depth is taken as the time of the departure from high stack amplitudes, before the first zero transit of the migrated energy. Fig. 6 shows the location of the reflectors in an amplitude–depth profile (Fig. 6d), which is in good agreement with the cross-sections (Figs 6b and c).

Fig. 7 shows the migrated sections with the amplitude–depth profiles for synthetic data calculated using the reflectivity method (Müller 1985) to compare to the data example shown in Fig. 6 using a model with a 3 per cent negative and a 1 per cent positive velocity increase at 2605 km depth. We produce velocity seismogram sections using the same source parameters (focal mechanism, depth and station configuration) as for the earthquake shown in Fig. 6. The velocity gradient in the models is slightly altered since we keep the velocity of ak135 at the CMB. The reflector depth is picked at the lower end of the positive (top row) and negative (bottom row) amplitude, respectively. The picks for D″ depths are consistent with the picks of *PcP*, which is taken to be the lower end of the large negative amplitude. The depths of both *PcP* and the D″ reflection agree well with the depths of the discontinuities in the synthetic models. Models with a small negative contrast of −1 per cent were also tested, which are more comparable to the predicted velocity contrasts from mineral physical models (Wookey *et al.* 2005). Although a small signal from such a small discontinuity can be detected in the data, it is close to the detection limit and likely not observable in real data. Since the data show clear detections for *P* waves in our data set, we conclude that the D″ discontinuity in this location is likely stronger than proposed by Wookey *et al.* (2005).

To test the reliability of our picks we used a well populated bin of the real data and took eight subsets of the traces for the migration. All subsets detected the same discontinuities as the full data set, indicating the stability of the detected structure. This test falls short of a full bootstrap analysis of the data, but the detection of the discontinuity with strongly decreased data volume indicates the robustness of the resolved structure. Additionally, we tested the reliability of the picks in the presence of noise. For this test we added noise to synthetic data. The noise was taken from the recorded data before the initial *P* arrival. The models include velocity contrasts of 3 per cent (positive and negative) at 2605 km depth. We find that even in synthetics with SNR of 0.5 (*PdP* amplitude to noise) the array processing is able to reliably detect the reflector at the correct depth.

Fig. 8 shows a second example for the event on 2001 April 21, which shows two reflectors above the CMB. In this example the CMB reflection is visible at 2915 km depth. A shallower strong reflector is visible at 2555 km depth. Additionally, a low-amplitude reflection can be detected at 2730 km depth. The shallower reflector
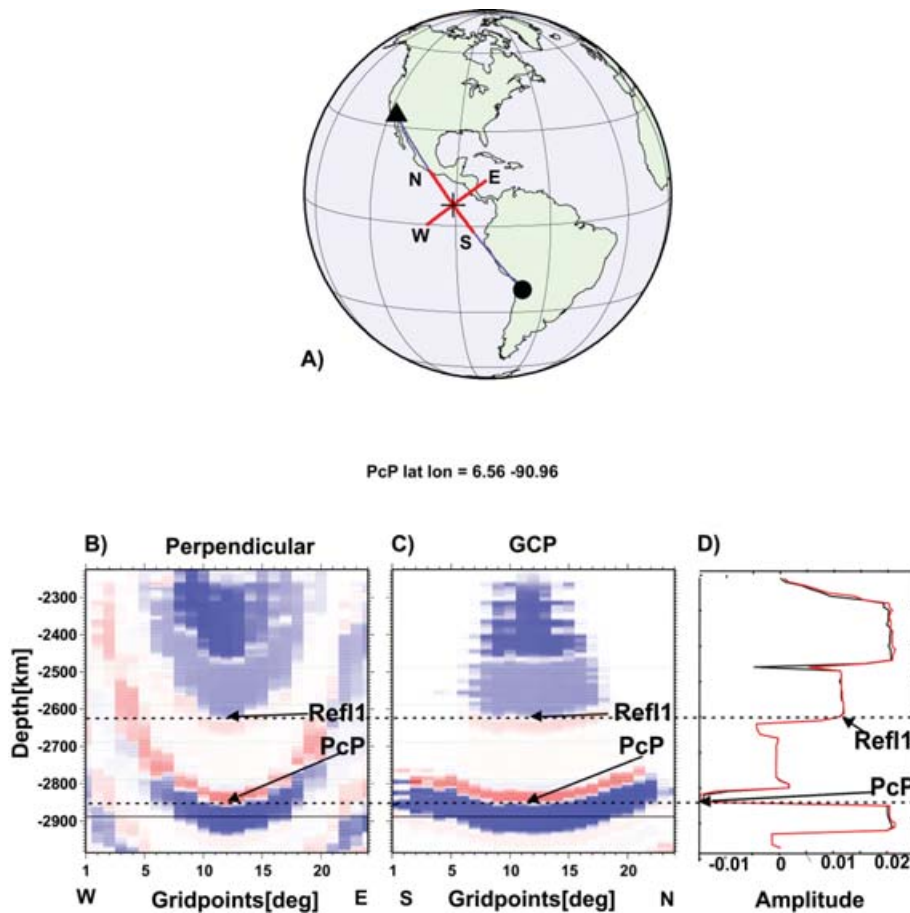
Figure 6. *P*-wave migration results in bin 5 of event on 2003 September 17. (a) Location of cross-section and source–receiver combination. The Migration result is shown in two cross-sections, perpendicular (b) and along (c) the great circle path at the *PcP* CMB reflection point and as amplitude–depth profile (d). In (a) and (b) *PcP* focuses as negative (red coloured) energy at about 2880 km depth. A positive (blue coloured) arrival is detected at 2635 km depth, with another positive arrival visible at 2480 km depth, this could be a remnant of the *P* wave. Energy mapping at depths less than 2500 km is most likely residue of the *P*-coda that did not get completely removed. (d) Amplitude–depth log for the same event, showing stacked amplitude as a function of depth in the migration in a column above the *PcP* reflection point. The reflection and *PcP* energy are indicated by arrows. The black line gives the stacked amplitude at the theoretical reflection point; the red line measures the amplitude in the 1 s Fresnel zone. Gridpoints are points on grid in the perpendicular and along the great circle path.

is hard to identify in the cross-sections but can easily be detected in the reflectivity profile emphasizing how the depth profiles and the cross-sections complement each other.

Using all bins of all earthquakes, we can produce a plan view map of the *P*-wave reflector depths (Fig. 9) where the reflector depth is indicated by colours. Similar to the DAM we detect two reflectors in the migrated data. Fig. 9 shows the reflection from CMB depth (top left), a lower reflector (top right) as well as the upper reflector (bottom left). The upper reflector is at an average depth of 2585 km with relatively strong topography. The lower reflector is more pronounced in the northern part of the sampled area, with depths between 2700 and 2835 km. The reflector depth seems to increase towards the south. We also see evidence for strong scattering (Liu *et al.* 1998) as indicated by strong depth variation of the reflector over short distance ranges.

The results from the migration method have been averaged in 1° latitudinal bins and the results have been added to Fig. 5(b) to compare the depths of the reflectors found with both methods. The upper reflector depth agrees well in both methods, however, there are some differences for the lower reflector depth between the DAM and the migration methods. In the northern part of the imaged area, the

detections are similar but towards the South the migration detects a deeper reflector than the DAM. The high amplitudes of the DAM detection for the lower reflector show a large smearing over a large depth range, possibly due to the averaging process of bins in the latitudinal and longitudinal direction. In addition, we do detect large topography in the migration along 5° latitude, which could lead to a mislocation of the reflector in the DAM.

We note that the implication for strong topography on the CMB is a mismapping of D″ velocity heterogeneity onto CMB depth. Since we use *P* as a reference phase, any velocity variations below the *P* turning point will map directly into *PcP* traveltime and, therefore, into CMB depth. The same effect can be observed in the stack for the DAM. The apparent CMB topography can also be observed in the synthetic tests shown in Fig. 7, where the different velocity structure for D″ results in a variation of apparent depth of the CMB. Studying the CMB variations would allow to estimate D″ and lower mantle velocity variations. Assuming small-scale topography on the CMB (Rost & Revenaugh 2004), mapping of CMB depths from *PcP* traveltimes could be used to estimate these D″ and lower mantle velocity heterogeneities. However, this has not been attempted in this study.
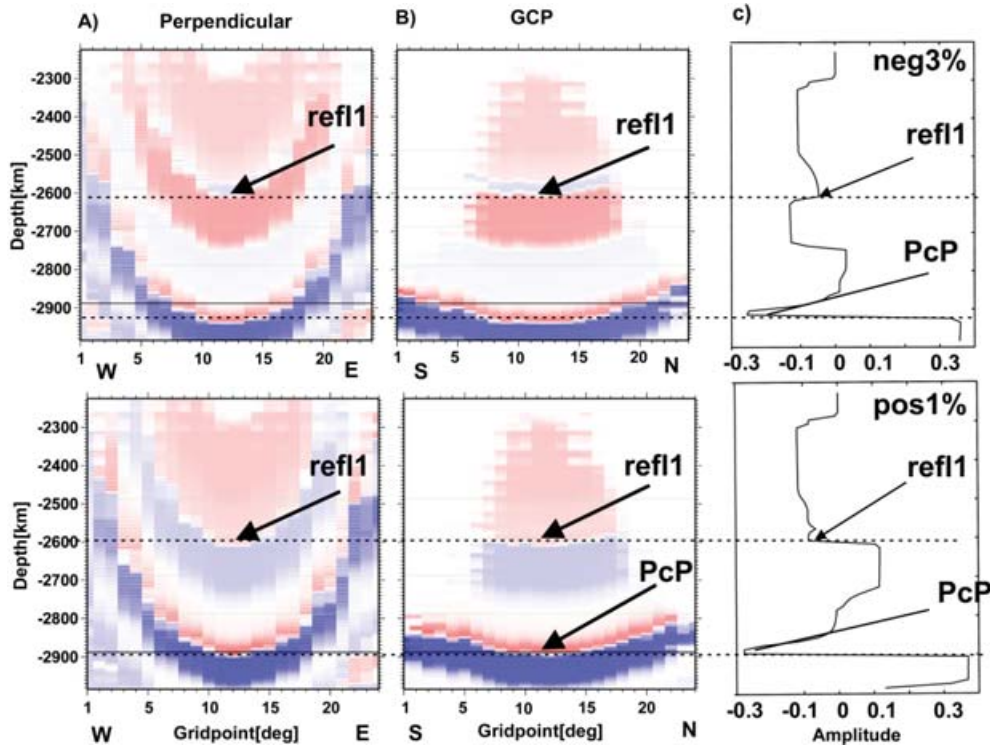
Figure 7. Synthetic data for a negative and a positive reflector in the *P*-wave velocity migrated the same way as for the event in Fig. 6. The top figure show the case for a negative reflector (perpendicular, along the great circle path and the amplitude depth profile) and the bottom row shows results for a positive *P*-wave velocity contrast at 2605 km depth.
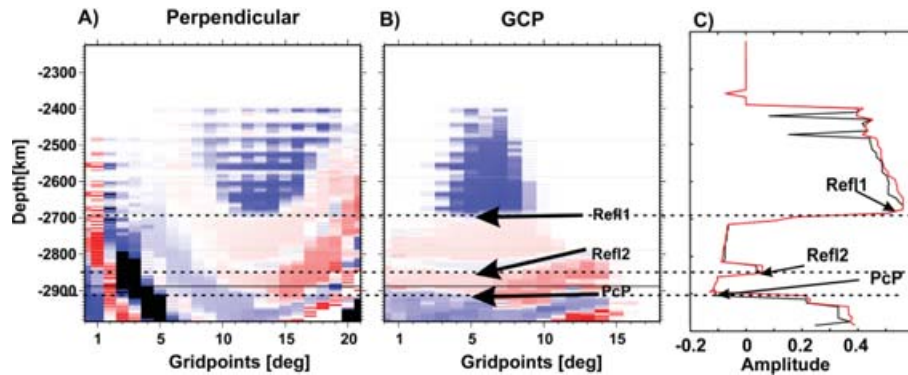

Figure 8. *P*-wave migration for bin 1 of event on 2001 April 21. Two reflectors can be detected in the migrated image. The two cross-sections and the amplitude–depth profile are as in Fig. 6 but a second lower reflector can be observed in all three panels.

3 WAVEFORMS

Using *PdP* and *SdS* waveforms we can study the velocity contrast of the reflectors in D″ by comparing the waveforms of *SdS* and *S* and *PdP* and *P*. A comparison of *PdP* and *P* waveforms is shown in Fig. 10. For both examples, the *P* wavelet is a two sided wavelet with a down-swing followed by an up-swing. The *PcP* waves show the same waveform as the *P* waves, however, the *PdP* wavelet clearly shows opposite polarity to the *P* and *PcP* waves. The same behaviour can also be seen in the vespagrams and the stack for *PdP* slowness and backazimuth. In general, the reflection depth profiles support the wavelet observation (compare Figs 6 and 8).

We calculate synthetic seismograms using the reflectivity method (Müller 1985) to study the influence of different reflector polarities on the waveforms. Results for three different models are shown in

Fig. 11. We show vespagrams on the left-hand side and the beam trace for *PdP* slowness in the middle panel with the model that was used in the right column. Due to slowness differences the *P* and *PcP* waveforms will be distorted in the beams for *PdP* slowness (e.g. the ramp on the *P* wave in the lower right figure). The *PdP* waveform in the data is best correlated to the synthetics for a negative velocity jump, as the polarity of the *PdP* wavelet seems to be opposite to the *P* and *PcP* wavelet. We therefore, conclude that the upper reflector has a negative *P*-velocity jump. Comparing the polarity of the stacked waveform for the second, deeper reflector phase estimated by the DAM analysis to the *P* and *PcP* wavelet, we find evidence for a positive velocity jump, which would account for the large amplitudes of this reflected wave in the DAM and migration. The *S*-wave data (Fig. 12) show a very different behaviour with a positive correlation of the waveform with *ScS* at the upper reflector and an opposite
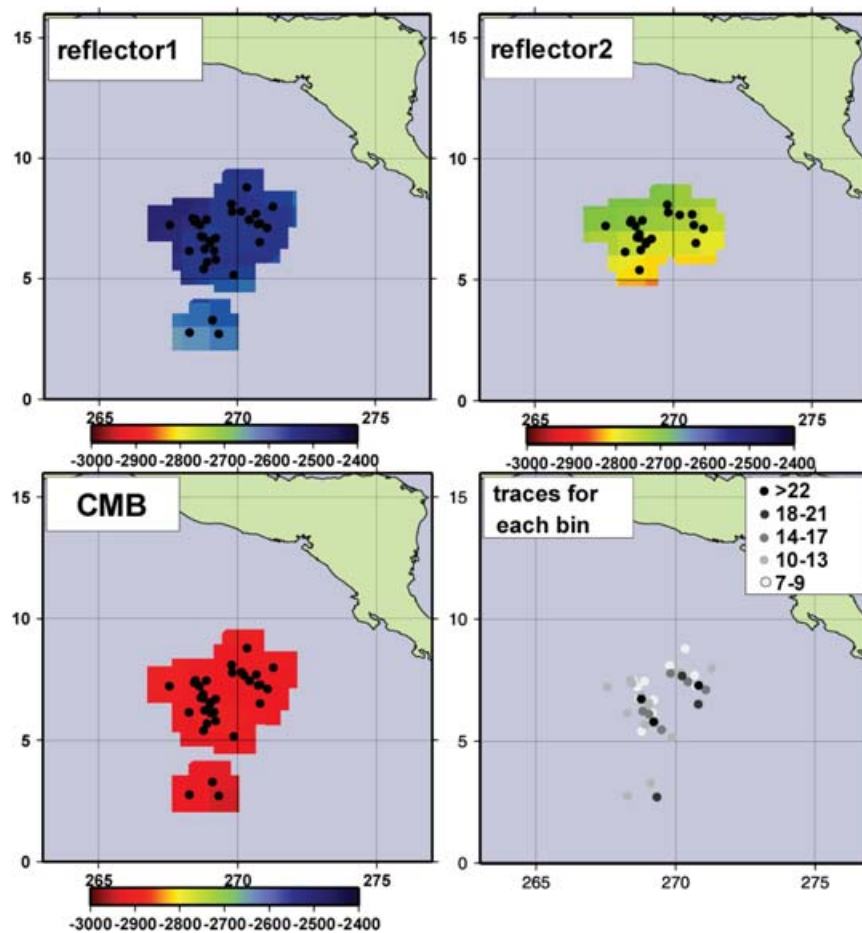
Figure 9. Results of the *P*-wave migration in map view. Bottom left-hand panel shows the CMB depth from the migration images, a slight depth trend is visible from south to north. The top right-hand panel shows the location of the deeper reflector (reflector 2), the reflector dips from 2700 km in the North to approximately 2800 km in the middle part of our study area. The top left panel shows that the detected shallow reflector (reflector 1) dips from about 2550 km in the north to about 2650 km in the south. Its average depth is 2585 km. There is stronger topography on this structure compared to the deeper reflector (reflector 2). The black circles indicate reflection points for the reference station for each bin. The bottom right figure indicates the number of traces used in each bin for the analysis.

waveform for the lower reflector in agreement with (Thomas *et al.* 2004, 2004b).

The negative upper reflector for *P* and positive upper reflector for *S* waves agree well with the results from Wookey *et al.* (2005), where a negative *P*-wave velocity contrast is predicted for the post-perovskite phase transition, in contrast to the often observed positive *S* wave contrast. The velocity contrast in Wookey *et al.* (2005) is predicted to be −0.51 per cent with an uncertainty due to temperature and pressure assumptions, but it is only likely to vary between −1 and 0 per cent for most temperature models of the lower mantle (Wookey, personal communication 2006). Using this prediction in the synthetic tests we find that although we see a small signal from the −1 per cent velocity jump, detection is difficult since the signal is at the detection limit. In our data set the signal from the upper reflector, therefore, suggests that the *P*-wave velocity jump is larger than −1 per cent and likely to be close to −3 per cent. The difference in the velocity contrast to Wookey *et al.* (2005) could be due to a different bulk modulus, density assumption, chemical material or different pressure (depth) range in their work. If we estimate a temperature based on their *P–T* diagram, our observation might indicate that the temperature is cooler than average in this area, but more seismological and mineralogical data would be necessary to get reliable physical properties in the lower mantle.

4 DISCUSSION

In this study, we compared two array methods applied to broad-band *P*- and *S*-wave data targeting a region of the lower mantle beneath the Cocos Plate. Due to the small amplitudes of the D″ reflections (especially for *P* waves), array methods are necessary to detect and model the subtle wavefield effects from possible lowermost reflections. Nonetheless, any study comparing *P*- and *S*-wave structure is confronted with some issues regarding the resolution of lower mantle structure. Seismic shear wave anisotropy has been modelled in this region of the Earth (Kendall & Nangini 1996; Kendall & Silver 1998; Garnero *et al.* 2004; Rokosky *et al.* 2004, 2006), from observations of shear wave splitting. Traveltime variation due to anisotropy can affect the mapping of D″ reflector depths. This could lead to a lack of correlation between the resolved *P*- and *S*-wave structure (though the effects of *P*-wave anisotropy are difficult to assess and have not been documented). Furthermore, strong lateral variations in D″ anisotropy can result in variable *ScS* splitting, and thus variable *ScS* time shifts on the *SH* component, resulting in defocusing of *ScS* in stacked traces.

We use direct *P* and *S* waves as reference phases and align all traces on these arrivals. Although this differential analysis procedure attempts to minimize traveltime perturbations due to
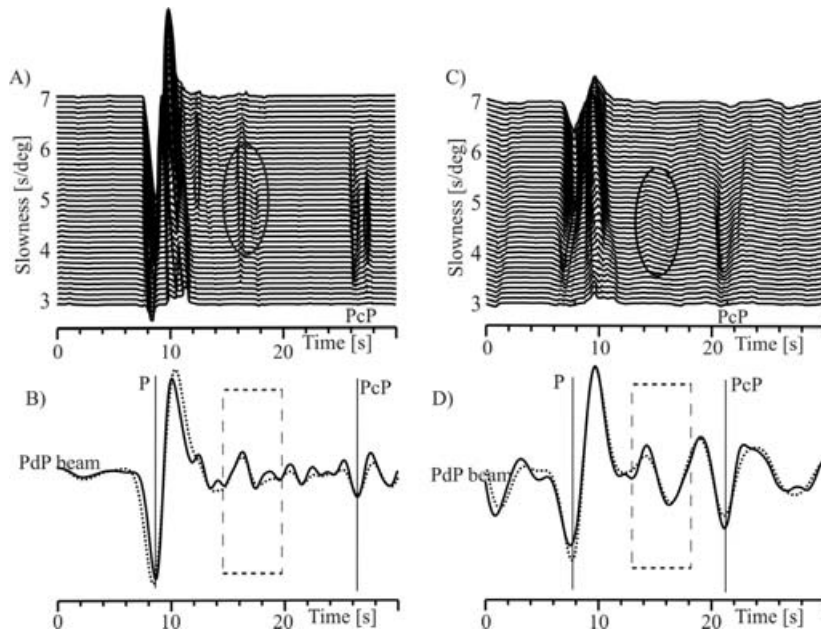
Figure 10. Waveform comparisons for *PcP* and *PdP*. The left hand side shows a fourth-root vespagram (a) and a fourth-root *PdP* beam trace (solid line) and a linearly stacked *PdP* beam trace (dotted line) for *PdP* slowness (b) for bin 5 for the event 2003 September 17, the right hand side shows the fourth-root vespagram (c) and fourth-root beam trace (solid line) and a linearly stacked *PdP* beam trace (dotted line) for *PdP* slowness (d) for bin 2 event 2000 June 14. The *PdP* reflection shows an opposite polarity compared to *P* and *PcP*. Figs (b) and (d) are summation traces (*PdP* beams) after shifting all traces in the seismogram section with the appropriate slowness and backazimuth for *PdP*. The *PdP* wavelet is marked by the dashed box.
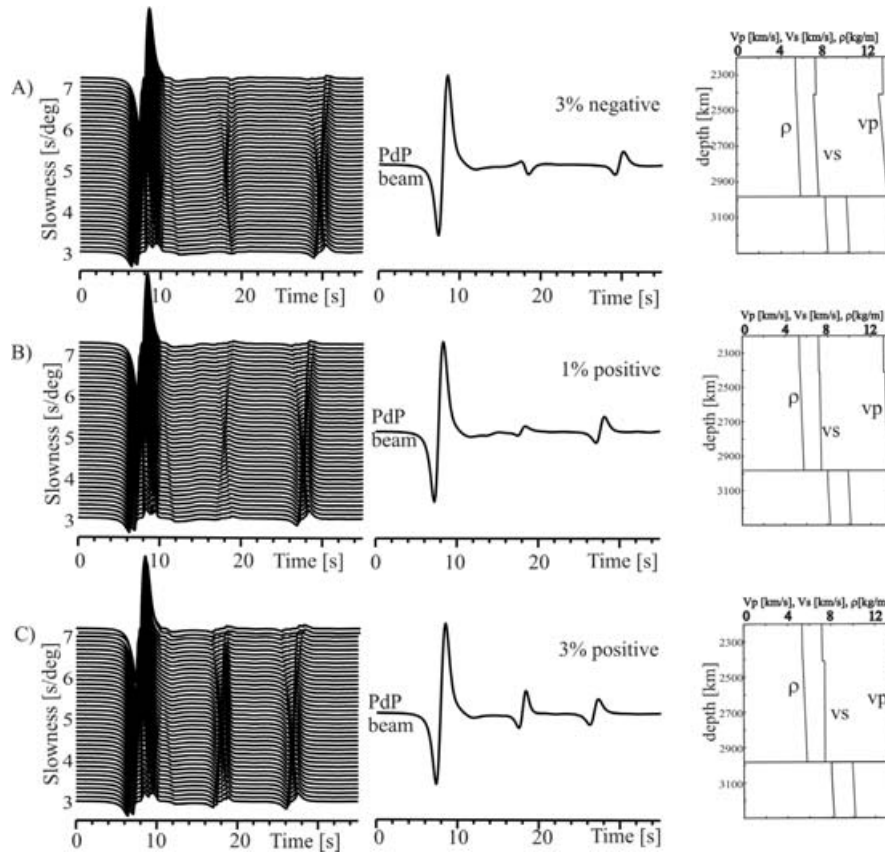

Figure 11. Vespagrams (left) and *PdP* beams (middle) (as Fig. 10) and models (right) for the synthetic data calculated for bin 5 event 2003 September 17. Top row: ak135 with an added negative velocity (−3 per cent) discontinuity in *P* and *S* at depth 2605 km. Middle row: ak135 with a positive (+1 per cent) velocity jump. Bottom row: ak135 with a positive (+3 per cent) velocity contrast. The *PdP* phase can clearly be seen in both vespagrams and *PdP* beams. The polarity of the *PdP* wave for the negative discontinuity model is similar to the waveform detected in the data. The *PcP* arrival time changes slightly due to the velocity model beneath the discontinuity in the synthetic models.
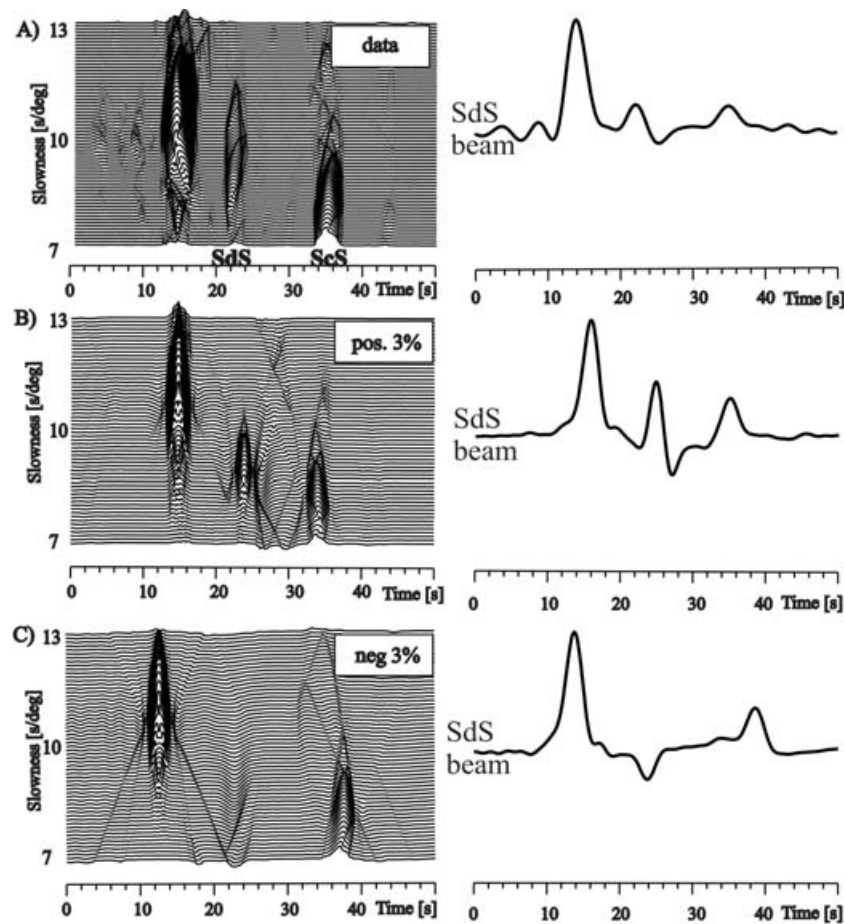
Figure 12. Waveforms in a vespagram and beam trace and synthetic models for the *S*, *SdS* and *ScS* wave. (a) Vespagram and beam trace for the event 1999 September 15. The waveforms of all three phases show the same polarity and suggest a positive velocity jump in D″. (b) Results from modelling with a positive *S*-wave jump at 2605 km depth. (c) Same as (b) but for a 3 per cent negative velocity jump in *S*.

heterogeneities beneath the receiver and source regions, heterogeneities in the mid and lower mantle may uniquely perturb the timing of the relatively shallow turning reference *P* and *S* wave. We therefore, employ a further correction whereby records are shifted by traveltime perturbation predictions from tomographic models before stacking. However, the applied corrections do not fully account for observed timing shifts, as is obvious from the CMB being mapped to incorrect depths.

We use traveltime predictions from 1-D ray tracing to 1-D earth models in our array stacking techniques. Velocity variations along the ray path will influence both the ray path itself and the predicted traveltime. Using 3-D ray tracing through high-resolution tomographic models will help to solve this problem. Nonetheless, the current tomographic models of this region do not capture the mantle structure in sufficient detail to warrant this kind of analysis.

The application of different array methods to the same data set leads to the detection of very similar structures. The reflector topography (Figs 5 and 9) from both methods is very similar and the different structures for *P* and *S* waves seem to be well resolved and stable (Fig. 5). The PWSEMBP method applied to *S* waves shows a discontinuity with a step at 4°N in good agreement with results from Thomas *et al.* (2004b), and Hutko *et al.* (2006). A second discontinuity can be detected and probably corresponds to the deeper reflector described in Thomas *et al.* (2004b). However, looking at the same *S*-wave data set, Hutko *et al.* (2006) find that these waves

map into an out-of-plane reflector. With our DAM method we are not able to detect out of plane scatterers, however, the migration method can potentially show out of plane reflections. We do not find evidence for consistent out of plane reflections in our *P*-wave data set. Furthermore, re-analysing the *S*-wave data set from Thomas *et al.* (2004b) did not lead to consistent out of plane reflections that could explain the lower reflector.

In general, the detected locations and depths for the reflectors from PWSEMBP are in very good agreement with the results from the migration method. Our waveform study and the comparison with synthetic seismograms indicate that the shallower *P*-wave reflector has a negative velocity contrast compared to the positive velocity contrast that is found for *S*-wave data. This is in good agreement with results from Wookey *et al.* (2005) for the post-perovskite phase transition (Murakami *et al.* 2004; Oganov & Ono 2004; Tsuchiya *et al.* 2004). Wookey *et al.* (2005) find that the combination of a reduction of bulk sound speed and a positive *S*-wave contrast across the post-perovskite phase transition leads to a small negative *P*-wave jump of 0.51 per cent. Our modelling of *P*-wave velocity jumps shows that a −1 per cent *P*-wave discontinuity is close to the detection limit of the data. The reliable detection of such a discontinuity suggests a larger *P*-wave contrast for the D″ discontinuity in this location.

Alternative models for the generation of the D″ discontinuity exist. A reflection from a folded slab (Christensen & Hofmann 1994) would lead to positive velocity steps for both *P* and *S* wave.

Reflections from the top and the bottom of the former slab could also explain the detection of two reflectors (Thomas *et al.* 2004). On the other hand, the two reflectors could be explained by a double crossing of the geotherm into and out of the post perovskite stability field (Hernlund *et al.* 2005). In this scenario, the lower *P*-wave reflector could show a positive velocity jump, which would explain the amplitudes above the noise level despite the velocity change smaller than ∼1 per cent that are observed for the *P* waves, due to critical reflections.

Although *P*- and *S*-wave velocity jumps across the D″ discontinuity predicted from the post-perovskite phase transition explain our observation favourably, the strong topography of the discontinuity is difficult to explain by the post-perovskite phase transition, since the depth of the phase transition mainly depends on the temperature in the lowermost mantle. The strong topography would require very strong lateral temperature gradients. Hutko *et al.* (2006) explain this difference in reflector depth with downwellings piles of a folding slab. It could also be speculated that the cause for the discontinuity in the southern part might be different from the northern part but clearly more research is required to provide an explanation for the observed strong topography.

Another issue we have to consider in this context is the fact that *P*-wave anisotropy might affect the polarity of the observed *PdP* waves and influence the interference of *PdP* and *PDP*. Unfortunately, *P*-wave anisotropy in the D″ is not unequivocally constrained, and mineral physics predictions of it at the present time depend on many uncertain parameters. It is not conceivable that randomly oriented *P*-wave anisotropy could reverse the polarity of the reflected wave, therefore, the polarity uncertainties may be related to the systematic *P*-wave anisotropy. We cannot discuss this issue thoroughly in this paper. However, this will be an important issue in future studies.

5 CONCLUSIONS

We investigated seismic structure of the D″ discontinuity beneath the Cocos plate using two different array stacking methods, that is, PWSEMBP and migration. We find strong coherence between the results of the PWSEMBP and migration methods, despite the different processing algorithms. Using PWSEMBP we detect a step-like change in D″ discontinuity depth around 4°N latitude, both in the *P*- and *S*-wave results. The 3-D migration approach also shows evidence for topography in east–west direction, although this topography shows a gentler gradient than detected by PWSEMBP. The amplitude of reflector topography along the N–S axis at 270 ± 5° in longitude is about 100 km with a change from about 2600 to 2700 km for *S* waves and from 2580 to 2700 km for *P* waves. There seems to be only one reflector visible in the *P*- and *S*-wave data south of 5°N, but at higher latitudes both methods suggest two discontinuities. Comparing waveforms of *P*- and *S*-wave reflections from the upper reflector suggests a negative velocity contrast for *P* waves but a positive contrast for *S* waves in good agreement with predictions from mineral physical calculations (Wookey *et al.* 2005). This makes the post-perovskite phase change a likely explanation for the reflectors observed in our data.

REFERENCES

Becker, T.W. & Boschi, L., 2002. A comparison of tomographic and geodynamic mantle models, *Geochem., Geophys., Geosys.*, **3**, doi:2001GC000168.

Boschi, L. & Dziewonski, A.M., 1999. High- and low-resolution images of the Earth's mantel: implications of different approaches to tomographic modeling, *J. Geophys. Res.*, **104**, 25 567–25 594.

Braña, L. & Helffrich, G., 2004. A scattering region near the core-mantle boundary under the North Atlantic, *Geoph. J. Int.*, **158**, 625–636.

Buffett, B.A., Garnero, E.J. & Jeanloz, R., 2000. Sediments at the top of Earth's core, *Science*, **290**, 1338–1342.

Castle, J.C., Creager, K.C., Winchester, J.P. & van der Hilst, R.D., 2000. Shear wave speeds at the base of the mantle, *J. Geophys. Res.*, **105**, 21 543–21 557.

Christensen, U.R. & Hofmann, A.W., 1994. Segregation of subducted oceanic crust in the convecting mantle, *J. Geophys. Res.*, **99**, 19 867–19 884.

Davies, D., Kelly, E.J. & Filson, J.R., 1971. Vespa process for analysis of seismic signals, *Nat. Phys. Sci.*, **232**, 8–13.

Ding, X.M. & Helmberger, D.V., 1997. Modeling D″ structure beneath Central America with broadband seismic data, *Phys. Earth planet. Inter.*, **101**, 245–270.

Dziewonski, A.M. & Anderson, D.L., 1981. Preliminary Reference Earth Model. *Phys. Earth planet. Int.*, **25**, 297–356.

Earle, P.S. & Shearer, P.M., 1997. Observations of PKKP precursors used to estimate small-scale topography on the core-mantle boundary, *Science*, **277**, 667–670.

Grand, S.P., 2002. Mantle shear-wave tomography and the fate of subducted slabs, *Phil. Trans. R. Soc Lond., A*, **360**, 2475–2491.

Grand, S.P., van der Hilst, R.D. & Widiyantoro, S., 1997. Global seismic tomography: a snapshot of convection in the Earth, *GSA Today*, **7**(4), 1–7.

Garnero, E.J., 2000. Heterogeneity of the lowermost mantle, *Annu. Rev. Earth planet. Sci.*, **28**, 509–537.

Garnero, E.J. & Lay, T., 2003. D″ shear velocity heterogeneity, anisotropy and discontinuity structure beneath the Caribbean and Central America, *Phys. Earth planet. Inter.*, **140**, 219–242.

Garnero, E.J., Maupin, V., Lay, T. & Fouch, M.J., 2004. Variable azimuthal anisotropy in Earth's lowermost mantle, *Science*, **306**, 5694.

Gu, Y.J., Dziewonski, A.M., Su, W. & Ekström, G., 2001. Models of the mantle shear velocity and discontinuity in the pattern of lateral heterogeneities, *J. Geophys. Res.*, **106**, 11 169–11 199.

Helffrich, G., 2002. Chemical and seismological constraints on mantle heterogeneity, *Phil. Trans. R. Soc Lond., A*, **360**, 2493–2505.

Hernlund, J.W., Thomas, C. & Tackley, P.J., 2005. A doubling of the post-perovskite phase boundary and the structure of the lowermost mantle, *Nature*, **434**, 882–886.

Hutko, A., Lay, T., Revenaugh, J., Garnero, E.J., 2006. Seismic detection of folded, subducted lithosphere at the core-mantle boundary, *Nature*, **441**, 333–336.

Karasón, H. & van der Hilst, R.D., 2001. Tomographic imaging of the lowermost mantle with differential times of refracted and diffracted core phases (PKP, Pdiff), *J. Geophys. Res.*, **106**, 6569–6587.

Kendall, J.M., 2000. Seismic Anisotropy in the Boundary Layers of the Mantle, in Earth's Deep Interior, in *Mineral Physics and Tomography From the Atomic to the Global Scale*, pp. 133–159, eds Karato, S., Forte, A.M., R.C. Liebermann, Masters, G. & Stixrude, L., AGU, Washington, DC.

Kendall, J.M. & Nangini, C., 1996. Lateral variations in D″ below the Caribbean, *Geophys. Res. Lett.*, **23**, 399–402.

Kendall, J.M. & Shearer, P.M., 1994. Lateral variations in D″ thickness from long-period shear wave data, *J. Geophys. Res.*, **99**, 11 575–11 590.

Kendall, J.M. & Silver, P.G., 1996. Constrains from seismic anisotropy on the nature of the lowermost mantle, *Nature*, **381**(6581), 09–412.

Kendall, J.M. & Silver, P.G., 1998. Investigating causes of D″ anisotropy, in *The Core-Mantle Boundary Region*, Geodyn. Ser., 28, pp. 97–118, eds Gurnis, M., Wysession, M.E., Knittle, E. & Buffett, B.A., AGU, Washington, DC.

Kennett, B.L.N., Engdahl, E.R. & Buhland, R., 1995. Constrains on seismic velocities in the Earth form travel-times, *Geophys. J. Int*, **122**, 108–124.

Kito, T. & Krüger, F., 2001. Heterogeneities in D″ beneath the southwestern Pacific inferred from scattered and reflected *P*-waves, *Geophys. Res. Lett.*, **28**, 2245–2548.

Kito, T., Krüger, F. & Negishi, H., 2004. Seismic heterogeneous structure in the lowermost mantle beneath the southwestern Pacific, *J. Geophys. Res.*, **109**, B09304, doi:10.1029/2003JB002677.

Krüger, F., Scherbaum, F., Weber, M. & Schlittenhardt, J., 1996. Analysis of asymmetric multipathing with a generalization of the double-beam method, *Bull. seismol. Soc. Am.*, **86**, 737–749.

Krüger, F., Weber, M., Scherbaum, F. & Schlittenhardt, J., 1995. Evidence for normal and inhomogeneous lowermost mantle and core-mantle boundary structure under the Arctic and northern Canada, *Geophys. J. Int.*, **122**, 637–657.

Lay, T. & Young, C.J., 1996. Imaging scattering structures in the lower mantle by migration of long-period S waves, *J. Geophys. Res.*, **101**, 20 023–20 040.

Lay, T. & Helmberger, D.V., 1983. A lower mantle *S*-wave triplication and the shear velocity structure of D″, *Geophys. Astron, J.R.,. Soc.,* **75**, 799–837.

Lay, T. & Garnero, E.J., 2004. Core-mantle boundary structures and processes, in *The State of the Planet: Frontiers and Challenges in Geophysics*, IUGG Volume 19, eds Sparks, R.S.J. & Hawkesworth, C.J., Geophysical Monograph 150, AGU, Washington, DC. doi:10.1029/150GM04.

Lay, T., Williams, Q. & Garnero, E.J., 1998. The core-mantle boundary layer and deep Earth dynamics, *Nature*, **392**, 461–468.

Lay, T., Garnero, E.J. & Williams, Q., 2004a. Partial melting in a thermo-chemical boundary layer at the base of the mantle, *Phys. Earth planet. Int.*, **146**, 441–467.

Lay, T., Garnero, E.J. & Russell, S.A., 2004b. Lateral variation of the D″ discontinuity beneath the Cocos plate, *Geophys. Res. Lett.*, L15612, doi:10.1029/2004GL020300.

Lay, T., Heinz, D., Ishii, M., Shim, S.-H., Tsuchiya, J., Tsuchiya, T., Wentzcovitch, R. & Yuen, D., 2005. Multidisciplinary Impact of the Deep Mantle Phase Transition in Perovskite Structure, *Eos Trans.*, **86**(1), 1–15.

Liu, X.-F., Tromp, J. & Dziewonski, A.M., 1998. Is there a forst-order discontinuity in the lowermost mantle?, *Earth planet. Sci. Lett.*, **160**, 343–351.

Lithgow-Bertelloni, C. & Richards, M.A., 1998. The dynamics of cenozoic and Mesozoic plate motions, *Rev. Geophys.*, **36**, 27–78.

Masters, G., Laske, G., Bolton, H. & Dziewonski, A.M., 2000. The relative behaviour of shear velocity, bulk sound speed, and compressional velocity in the mantle: implications for chemical and thermal structure, in *Earth's Deep Interior: Mineral Physics and Tomography From the Atomic to the Global Scale*, pp. 63–87, eds Karato, S., Forte, A.M., Liebermann, R.C., Masters, G., Stixrude, L., AGU, Washington, DC.

Maupin, V., Garnero, E.J., Lay, T. & Fouch, M.J., 2005. Azimuthal anisotropy in the D″ layer beneath the Caribbean, *J. Geophys. Res.*, **101**, B08301, doi:10.1029/2004JB003506.

Mitchel, B.J. & Helmberger, D.V., 1973. Shear velocities at the base of the mantle from observations of S and ScS, *J. Geophys. Res.*, **78**, 6009–6020.

Murakami, M., Hirose, K., Sata, N., Ohishi, Y. & K Kawamura, 2004. Phase transition of MgSiO3 perovskite in the deep lower mantle, *Science*, **304**, 855–858.

Müller, G., 1985. The reflectivity method: a tutorial, *J. Geophys.* **58**, 153–174.

Oganov, A.R. & Ono, S., 2004. Theoretical and experimental evidence for a post-perovskite phase of MgSiO3 in Earth's D″ layer, *Nature*, **430**, 445–448.

Persh, S.T., Vidale, J.E. & Earle, P.S., 2001. Absence of short-period ULVZ precursors to PcP and ScP from two regions of the CMB, *Geophys. Res. Lett.*, **28**, 387–390.

Reasoner, C. & Revenaugh, J., 1999. Short-period P wave constraints on D″ reflectivity, *J. Geophys. Res.*, **104**, 955–961.

Revenaugh, J. & Meyer, R., 1997. Seismic evidence of partial melt within a possibly ubiquitous low-velocity layer at the base of the mantle, *Science*, **277**, 670–673.

Ritsema, J. & Van Heijst, H.J., 2000. Seismic imaging of structural heterogeneity in Earth's mantle: evidence for large-scale mantle flow, *Sci. Prog.*, **83**, 243–259.

Rokosky, J.M., Lay, T., Garnero, E.J & Russel, S.A., 2004. High-resolution investigation of shear wave anisotropy in D″ beneath the Cocos Plate, *Geophys. Res. Lett.*, **31**, L07605, doi:10.1029/2003GL018902.

Rokosky, J.M., Lay, T., Garnero, E.J., 2006. Small-scale lateral variations in azimuthally anisotropic D″ structure beneath the Cocos Plate, *Earth planet. Sci. Lett.*, **248**, 411–425.

Rost, S. & Revenaugh, J., 2001. Seismic detection of rigid zones at the top of the core, *Science*, **294**, 1911–1914.

Rost, S. & Thomas, C., 2002. Array Seismology: methods and Applications, *Rev. Geophys.*, **40**, 10.1029/2000RG000100..

Rost, S. & Revenaugh, J., 2003. Small-scale ultralow-velocity zone structure imaged by ScP, *J. Geophys. Res.*, **108**, 2056, doi:10.1029/2001JB001627.

Rost, S. & Revenaugh, J., 2004. Small-scale changes of core-mantle boundary reflectivity studied using core reflected PcP, *Phys. Earth planet. Int.*, **145**, 19–36.

Rost, S. & Garnero, E.J., 2004. Array seismology advances Earth interior research, *Eos Trans.*, **85**, AGU, **301**, 305–306.

Rost, S., Garnero, E.J., Williams, Q. & Manga, M., 2005. Seismic constraints on a possible plume root at the core-mantle boundary, *Nature*, **435**, 666–669 doi:10.1038/nature03620.

Scherbaum, F., Krüger, F., Weber, M., , 1997. Double beam imaging: mapping lower mantle heterogeneities using combinations of source and receiver arrays, *J. Geophys. Res.*, **102**(I), 507–522.

Schimmel, M. & Paulssen, H., 1997. Noise reduction and detection of weak, coherent signals through phase-weighted stacks, *Geophys. J. Int*, **130**, 497–505.

Sidorin, I., Gurnis, M. & Helmberger, D.V., 1999a. Evidence for a ubiquitous seismic discontinuity at the base of the mantle, *Science*, **286**, 1326–1331.

Sidorin, I., Gurnis, M. & Helmberger, D.V., 1999b. Dynamics of a phase change at the base of the mantle consistent with seismological observations, *J. Geophys. Res.*, **104**, 15 005–15 023.

Stammler, K., 1993. Seismic Handler—Programmable multichannel data handler for interactive and automatic processing of seismological analysis. *Comput. Geosci.*, **19**, 135–140.

Sun, D., Song, T.-R.A. & Helmberger, D., 2006. Complexity of D″ in the presence of slab-debris and phase changes, *Geophys. Res. Lett.*, **33**, L12S07, doi:10.1029/2005GL025384.

Taner, M.T. & Koehler, F., 1969. Velocity spectra-digital derivation and applications of velocity functions, *Geophysics*, **84**, 859–881.

Thomas, C., Weber, M., Wicks, C.W. & Scherbaum, F., 1999. Small scatterers in the lower mantle observed at the German broadband arrays, *J. Geophys. Res.*, **104**, 15 073–15 088.

Thomas, C., Kendall, J.-M. & Lowman, J., 2004a. Lower mantle seismic discontinuities and the thermal morphology of subducted slabs, *Earth planet. Sci. Lett.*, **255**, 105–113.

Thomas, C., Garnero, E.J. & Lay, T., 2004b. High-resolution imaging of lowermost mantle structure under the Cocos Plate, *J. Geophys. Res*, **109**, doi:10.1029/2004JB003013.

Thorne, M.S., Lay, T., Garnero, E.J., Jahnke, G. & Igel, H., 2006. 3-D seismic imaging of the D″ region beneath the Cocos Plate, *Geophys. J. Int.*, submitted

Tsuchiya, T., Tsuchiya, J., Umemoto, K. & Wentzcovitch, R.M., 2004. Phase transition in MgSiO3 perovskite in the earth's lower mantle, *Earth planet. Sci. Lett.*, **224**, 241–248.

Vidale, J.E. & Hedlin, M.A.H., 1998. Evidence for partial melt at the core-mantle boundary north of Tonga from the strong scattering of seismic waves, *Nature*, **391**, 682–684.

Weber, M. & Davis, J.P., 1990. Evidence of a laterally variable lower mantle structure from P and S waves, *Geophys. J. Int.*, **102**, 231–255.

Weber, M. & König, M., 1992. A search for anomalies in the lowermost mantle using seismic bulletins, *Phys. Earth planet. Int.*, **73**, 1–28.

Weber, M., 1994. Lamellae in D″?, An alternative model for lower mantle anomalies, *Geophys. Res. Lett.*, **21**, 2531–2534.

Wen, L., Silver, P., James, D. & Kuehnel, R., 2001. Seismic evidence for a thermo-chemical boundary at the base of the Earth's mantle, *Earth planet. Sci. Lett.*, **189**, 141–153.

Wessel, P. & Smith, W.H.F., 1995. New version of the Generic Mapping Tools released, *EOS Trans. AGU*, **76**, 329.

Williams, Q., Revenaugh, J.S., Garnero, E.J., 1998. A correlation between ultra-low basal velocities in the mantle and hot spots, *Science*, **281**, 546–549.

Wookey, J., Stackhouse, S., Kendall, J.M., Brodholt, J.P. & Price, G.D., 2005. Efficacy of the post-perovskite phase as an explanation of lowermost mantle seismic properties. *Nature*, **438**, 1004–1008.

Wysession, M.E., 1996. Imaging cold rock at the base of the mantle: the sometimes fate of Slabs?, in *Subduction: Top to Bottom*, pp. 369–384, eds Bebout, G.E., Scholl, D., Kirby, S., Platt, J.P., AGU, Washington, DC.

Wysession, M.E., Lay, T., Revenaugh, J., Williams, Q., Garnero, E.J., Jeanloz, R. & Kellog, L.H., 1998. The D″ discontinuity and its implications, in *The Core-Mantle Boundary Region*, Geodynam. Ser., 28, pp. 273–297, Buffett, B.A., AGU, Washington, DC.

Zhang, J. & Lay, T., 1984. Investigation of a lower mantle shearwave triplication using a broadband array, *Geophys. Res. Lett.,* **11**, 620–623.